

PAPER • OPEN ACCESS

## Scalable and cost-effective fabrication of high-performance self-powered heterojunction UV-photodetectors using slot-die printing of triple-cation lead perovskite coupled with triboelectric nanogenerators

To cite this article: Sajjad Mahmoodpour *et al* 2024 *J. Phys. Energy* **6** 015014

View the [article online](#) for updates and enhancements.

### You may also like

- [An enhancement on supercapacitor properties of porous CoO nanowire arrays by microwave-assisted regulation of the precursor](#)  
Yin Sun, Junjie Zhang, Sen Liu et al.
- [Enhancing the Phase Stability of Formamidinium Lead Triiodide by Addition of Calcium Chloride](#)  
Jin Hyuck Heo, Nang Mya Su Aung, Seok Yeong Hong et al.
- [Effect of plasma activated water treated by LF-microwave hybrid plasma on enhancement of seed germination and plant growth](#)  
Norrawit Tonmitr and Akira Yonesu



## PAPER

## OPEN ACCESS

RECEIVED  
8 September 2023REVISED  
28 October 2023ACCEPTED FOR PUBLICATION  
30 November 2023PUBLISHED  
7 December 2023

Original content from this work may be used under the terms of the [Creative Commons Attribution 4.0 licence](https://creativecommons.org/licenses/by/4.0/).

Any further distribution of this work must maintain attribution to the author(s) and the title of the work, journal citation and DOI.



# Scalable and cost-effective fabrication of high-performance self-powered heterojunction UV-photodetectors using slot-die printing of triple-cation lead perovskite coupled with triboelectric nanogenerators

Sajjad Mahmoodpour<sup>1</sup>, Leyla Shooshtari<sup>1</sup>, Nassim Rafiefard<sup>1</sup>, Raheleh Mohammadpour<sup>1,\*</sup> , Nima Taghavinia<sup>1,2</sup>  and Daryoosh Vashae<sup>3,\*</sup> 

<sup>1</sup> Center for Nanoscience and Nanotechnology, Institute for Convergence Science & Technology, Sharif University of Technology, Tehran, Iran

<sup>2</sup> Department of Physics, Sharif University of Technology, Tehran, Iran

<sup>3</sup> Electrical & Computer Engineering Department, North Carolina State University, Raleigh, NC 27606, United States of America

\* Authors to whom any correspondence should be addressed.

E-mail: [mohammadpour.raheleh@gmail.com](mailto:mohammadpour.raheleh@gmail.com) and [dvashae@ncsu.edu](mailto:dvashae@ncsu.edu)

**Keywords:** UV photodetector, slot-die printing, perovskite, triboelectric nanogenerator, self-powered device

Supplementary material for this article is available [online](#)

## Abstract

The demand for continuous monitoring of ultraviolet (UV) radiation, which poses significant health risks, has grown significantly with the advent of the internet of things (IoT) for human health. The need for a self-powered system that does not rely on battery charging in environmental conditions has led to the exploration of triboelectric nanogenerators (TENGs) as a promising energy source for sensor systems. In this study, we present a fully printed UV photodetector (UV-PD) that is fabricated through scalable slot-die printing of either single-layer triple-cation mixed halide perovskite (TCMHP) or a heterojunction of TiO<sub>2</sub>/TCMHP on patterned fluorine-doped tin oxide (FTO). The integrated TENG generates the required energy from the tapping of Kapton to the FTO contact, making the device self-powered. Our self-powered PD exhibits an excellent responsivity and detectivity of 71.4 mA W<sup>-1</sup> and 6.92 × 10<sup>10</sup> Jones, respectively, under a 395 nm wavelength, significantly outperforming spin-coated TCMHP-based devices. We further optimized the performance of our integrated TENG-powered heterojunction TiO<sub>2</sub>/TCMHP UV-PD by fabricating sensors with groove spacings of 2, 3, 5, and 8 mm. The optimized device demonstrated an unprecedented responsivity, detectivity, and EQE% of 151.9 mA W<sup>-1</sup>, 1.29 × 10<sup>11</sup> Jones, and 47.8%, respectively, under UV irradiation. Our work represents a significant step towards large-scale industrial flexible self-powered UV detection devices that can protect human health and safety. This study highlights the potential of scalable and cost-effective slot-die printing techniques for the industrial production of high-performance self-powered UV sensors, with significant implications for IoT-based health monitoring and environmental protection applications.

## 1. Introduction

Exposure to solar radiation is a significant public health concern as excessive exposure to certain wavelengths, such as ultraviolet (UV) radiation, can lead to various health problems, including skin cancer, eye damage, DNA damage, and accelerated aging [1–4]. UV-A radiation (320–400 nm) is particularly concerning among the different categories of UV radiation (UV-B, 290–320 nm, and UV-C, 320–400 nm) as it passes through the Earth's atmosphere, and human skin does not have adequate protection against it [5]. Additionally, UV rays are widely used in industries such as food, medicine, dentistry, and cosmetics, making their safe usage

imperative [6, 7]. Thus, the development of effective UV photodetectors (PDs) is crucial for monitoring UV irradiation. These devices convert UV illumination into electrical signals. To achieve a sensitive, selective, and stable optoelectronic device, a heterogeneous structure is required. This structure effectively separates charge carriers, thereby preventing recombination and leading to an increased optical response of the PD to high-energy photons and higher quantum efficiency [8, 9]. Perovskites are semiconductor materials with superior properties such as high absorption coefficient, low trap density, and long carrier diffusion length, making them ideal candidates for the development of UV PDs [10]. The conduction bands of the TiO<sub>2</sub> and TCHMPs heterojunctions match well, making them stable and responsive to UV irradiation [11–13].

Large-scale fabrication techniques are essential for commercializing PDs. Printing techniques such as injection printing, blade coating, spray coating, and slot-die coating are cost-effective and compatible with Roll-to-Roll (R2R) fabrication as a mass-production method [14–17]. Slot-die coating is particularly advantageous for forming a uniform thin film over large areas with a low waste of raw materials and fast coating capacity [18–21].

Smart manufacturing has gained popularity in recent years, with the internet of things (IoT) and artificial intelligence (AI) playing central roles. Sensors that convert external stimuli such as light, pressure, humidity, and temperature into electrical signals are critical components of these technologies [22]. However, traditional sensors that rely on external energy sources have limitations such as frequent charging needs, a limited life cycle, and high maintenance costs. Self-powered devices, including PDs integrated with wireless transmitters, are promising solutions for IoT applications [23, 24]. Nanogenerators (NGs) that convert ambient energy into electrical energy are ideal for powering these self-powered PDs. The most common NGs include piezoelectric NGs (PENG), triboelectric NGs (TENG), and pyroelectric NGs (PyNG), with the first two based on wasted and distributed mechanical stimuli [25]. TENGs, invented in 2012, have a higher power density compared to other NGs and operate based on the combined effect of contact electricity and electrostatic induction [26, 27]. Since various forms of wasted energy are not consistently available simultaneously, an ideal solution involves the development of hybrid harvesters that can capitalize on whatever waste energy is present in the environment. This approach not only utilizes all available waste energy sources but also enhances the overall efficiency of the harvester [28–30]. In response to the growing demand for a reliable energy source for self-powered electronic devices, the concept of hybridized NGs has emerged. These hybrid NGs are formed by combining two or more NGs, resulting in increased stability and effectiveness in energy harvesting. By bringing together different energy-harvesting systems, such as mechanical, solar, and thermal, hybrid NGs tap into the potential of coexisting energy sources. This synergy among diverse energy sources allows for the continuous generation of sustainable energy within a single integrated system [28–30].

TENG consists of two polymer sheets with distinct triboelectric properties: one with the ability to gain electrons and the other with the capacity to lose electrons. These sheets are stacked together, allowing them to slide relative to each other. When mechanical energy is harvested, it induces deformation in the insulating polymer sheets. This deformation causes the two sheets to come into contact and rub against each other, leading to the generation of charges on the internal surfaces of the polymer sheets due to the triboelectric effect and electrostatic induction. Consequently, this process results in the creation of an electrical potential difference on the electrodes attached to the triboelectric layers. Electrons flow from the lower potential side to the higher potential side to reach an equilibrium state, leading to the accumulation of electrostatically induced charges on the electrodes [31, 32]. TENGs exhibit four primary operational modes, each characterized by its unique structure and working principles. These modes include the vertical contact-separation mode, lateral sliding mode, single-electrode mode, and triboelectric-layer freestanding mode.

TENGs offer the remarkable capability to harness bioenergy in work environments characterized by a frequency range below 10 Hz, closely mirroring human physiological signals. This sensitivity can be further enhanced to detect subtle body deformations, effectively serving as a pressure sensor to monitor various aspects of human physiology. The versatility of TENG technology extends to a wide array of fields, where numerous researchers have concentrated their efforts on utilizing TENGs to capture ambient mechanical energy [31, 32]. This collective research effort has yielded three prominent directions: (a) Biomedical applications: in domains like human-machine interface development for security, safety, and robotics, TENGs are employed as self-powered sensors and systems, exemplifying their adaptability in healthcare and related areas. (b) Blue energy concept realization: TENGs have been effectively employed to harvest energy from water waves, contributing to the pursuit of sustainable energy generation through the concept of ‘blue energy.’ (c) Micro/nanopower generation: TENGs are leveraged as sustainable micro/nanopower sources to power small electronic devices autonomously, ensuring reliable and eco-friendly energy solutions. This multifaceted approach underscores the growing potential of TENGs as dependable sensors and energy harvesters across a wide spectrum of applications.

Several studies have explored the potential of self-powered perovskite PDs integrated with TENGs and PENGs. Su *et al* demonstrated an automated PD based on MAPBI<sub>3</sub>, serving as both the triboelectric and photoactive layer of the PD structure [33]. They reported a comprehensive study on the electron affinity of triboelectric layers in self-powered MaPbI<sub>3</sub>-based PDs through the selection of different polymer- and metal-based triboelectric layers [34]. Wang *et al* [35] presented a self-powered flexible perovskite-based PD powered by human finger tapping, demonstrating a high responsivity of up to 79.4 V per mW cm<sup>-2</sup> and a voltage response of 90% [36]. A recent report on a self-powered SnS<sub>2</sub>/TCHMP-based PD powered by a GO paper-based/Kapton TENG showed a light current ratio to a dark current of 300% [37]. Wang *et al* observed significant output after doping the CsPbBr<sub>3</sub> lattice in perovskite-PDs with Ba<sup>2+</sup> cations and powering them with TENGs, highlighting the potential of perovskite as a suitable candidate for use in mechanical and optical hybrid devices [38].

It is important to note that all perovskite-based photodetectors (PDs) are currently fabricated using non-scalable methods, underscoring the need for a scalable fabrication approach. In this study, we utilized the slot-die coating method to deposit and optimize the TCHMP layer for optimal absorption. We then fabricated a planar heterojunction TiO<sub>2</sub>/TCHMP UV PD using slot-die coating and a chemically etched fluorine-doped tin oxide (FTO) with varying groove sizes in millimeter ranges. The FTO connection was utilized as a NG along with a Kapton triboelectric layer, enabling the photodetector to function self-generated without the need for batteries. With a sensitivity of approximately 9500, our TiO<sub>2</sub>/TCHMP-based photodetector, fabricated through large-scale manufacturing, has one of the best records among perovskite-based photodetector structures. The proposed high-efficiency self-powered heterojunction PD coupled with the TENG has the potential to produce large-scale sensors for advanced technologies such as IoT.

## 2. Experimental section

To enable scalable slot-die printing of thin films, we constructed a custom machine incorporating a motorized X–Y table, a heater bed, and a high-precision syringe pump (figure 1). The X–Y table has been engineered for exceptional stability, while the heater bed has been fitted with high-precision heating elements, allowing for accurate temperature control within the range of room temperature to 240 °C. Moreover, the slot-die head, with a width of 30 mm, features a high-precision syringe pump capable of delivering an injection speed ranging from 25 μl min<sup>-1</sup> to 700 μl min<sup>-1</sup>. Our custom-built slot-die machine provides a pioneering solution for the high-precision, scalable, and cost-effective deposition of thin films, paving the way for the fabrication of cutting-edge optoelectronic devices.

### 2.1. Materials

The chemicals, including dimethylformamide anhydrous (DMF), dimethyl sulfoxide (DMSO), cesium iodide (CsI), formamidinium iodide (FAI), Zn powder, and HCl solvent, were purchased from Sigma Aldrich and Merck companies. PbI<sub>2</sub> 99.99%, PbBr<sub>2</sub> 99.99%, methylammonium bromide (MABr), and TiO<sub>2</sub> mesoporous paste were obtained from Sharif Solar Company. The perovskite precursor solution was prepared by mixing PbI<sub>2</sub> (1.1 M), PbBr<sub>2</sub> (0.22 M), FAI (1 M), and MABr (0.2 M) in a solvent mixture of anhydrous DMF and DMSO (4:1). The CsI standard solution (1.5 M) in DMSO was stirred overnight at room temperature and added to the precursor solution in an equal volume. The final precursor solution of triple cation lead perovskite (TCLP), Cs<sub>0.05</sub>(FA<sub>0.83</sub>MA<sub>0.17</sub>)<sub>0.95</sub>Pb(I<sub>0.83</sub>Br<sub>0.17</sub>)<sub>3</sub>, was stirred for half an hour under ambient conditions.

### 2.2. Device fabrication and measurement

#### 2.2.1. Substrate preparation

FTO-coated glass substrates (with TCO30-10, 10 Ω sq<sup>-1</sup> conductivity) were cut to dimensions of 12 cm × 2.8 cm and 1.4 cm × 2.8 cm. Initially, they were cleaned with a detergent solution in an ultrasonic bath for 10 min, rinsed with deionized water, and subsequently cleaned with acetone and isopropanol in an ultrasonic bath for an additional 10 min. After rinsing and drying under compressed air, the substrates were treated with UV ozone.

#### 2.2.2. Optimized fabrication of the perovskite-based UV photodetector

The process of fabricating the planar photodetector is shown in figure 2. It involved chemically etching the FTO crystalline layer on the FTO/glass substrate using Zn powder and HCl [35]. Grooves of fixed widths (3 mm, 5 mm, and 8 mm) were created in the center of the substrate using a mask made from Scotch<sup>®</sup> Magic<sup>™</sup> Tape. The surface was brushed after adding Zn powder and diluted HCl, then rinsed with DI water.

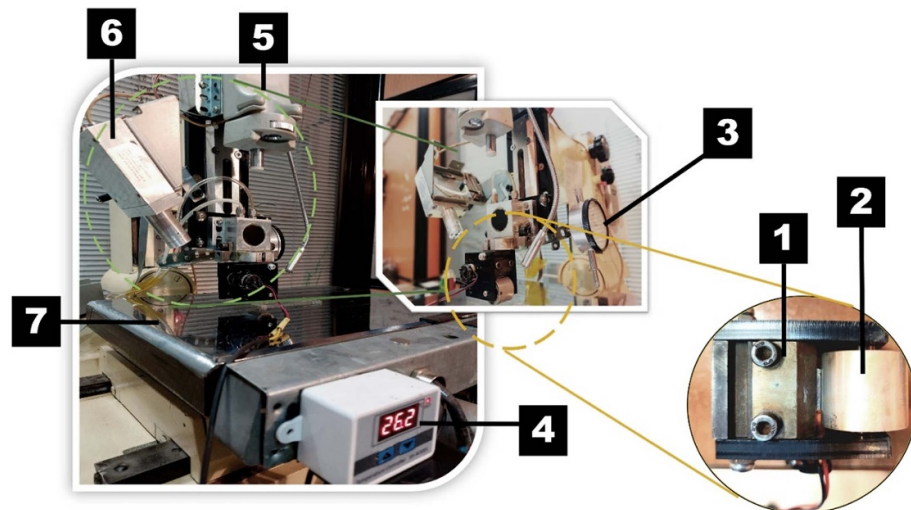


**Figure 1.** Our home-built slot-die coating machine, as illustrated, comprises the following components: (1) a slot-die head, (2) a roller coater, (3) a micrometer, (4) a bed temperature controller, (5) a syringe pump, (6) a laser for roughness measurement, and (7) a motorized X–Y table for precise positioning. With its high-precision syringe pump and temperature-controlled bed with a motorized X–Y table, this machine offers a versatile and cost-effective solution for the scalable deposition of thin films for various applications.

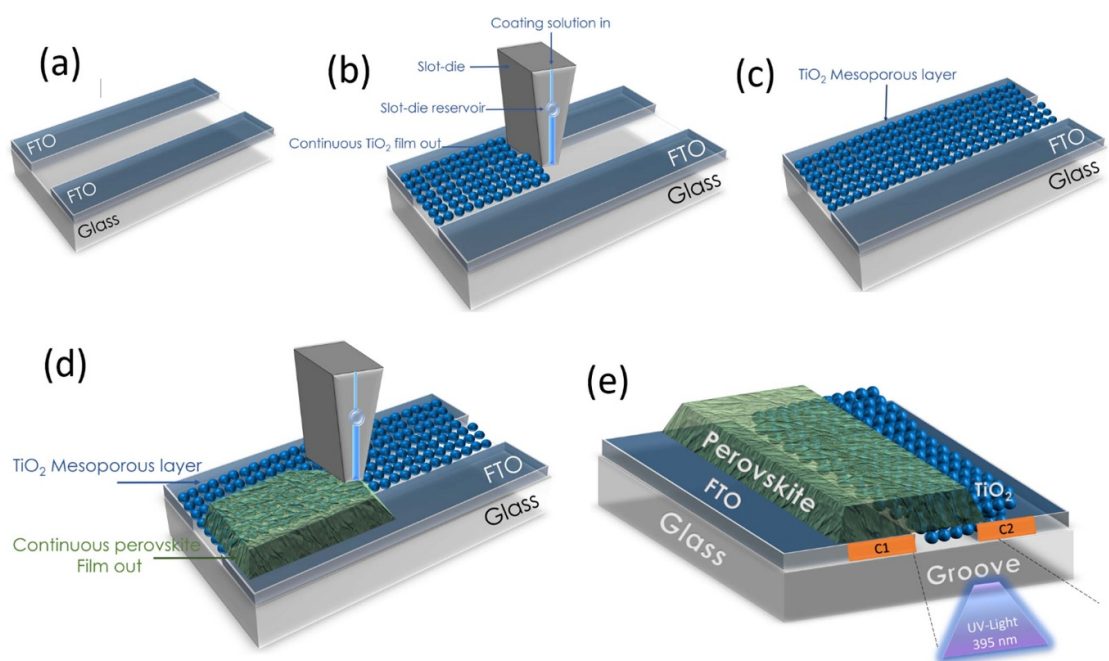


**Figure 2.** Schematic diagram illustrating the process of fabricating the heterojunction  $\text{TiO}_2$ /TCHMP photodetector using a slot-die printer: (a) chemical etching of grooves in the substrate using zinc powder and diluted HCl, (b) deposition of mesoporous  $\text{TiO}_2$  ( $\text{TiO}_2$  MP) layer on one side of the groove using the slot-die process, (c) fabrication of the  $\text{TiO}_2$  MP layer through the slot-die process, which covers only one side of the FTO/glass substrate, (d) deposition of the perovskite layer through the slot-die process, which covers the  $\text{TiO}_2$  layer as well as the other side of the FTO/glass substrate, and (e) the resulting heterojunction  $\text{TiO}_2$ /triple cation mixed halide perovskite under UV irradiation, C1: Perovskite/FTO contact and C2:  $\text{TiO}_2$ /FTO contact.

The deposition of  $\text{TiO}_2$  and perovskite layers was carried out using a homemade slot-die machine. The  $\text{TiO}_2$  paste was diluted with ethanol in a 1:5.5 ratio and stirred overnight. The  $\text{TiO}_2$  layer was deposited at a printing speed of  $1 \text{ cm s}^{-1}$ , with a head temperature of  $25 \pm 5 \text{ }^\circ\text{C}$ , and a substrate temperature of  $35 \pm 5 \text{ }^\circ\text{C}$ . The perovskite layer was deposited with a printing speed of  $1.2 \text{ cm s}^{-1}$ , with a head temperature of  $25 \pm 5 \text{ }^\circ\text{C}$ , and a substrate temperature of  $45 \pm 5 \text{ }^\circ\text{C}$ . Ag paste was placed on both sides of the printed substrate to form better electrical contacts. For the reference sample, the spin-coating method was used to fabricate the device. First, the FTO glass is etched in the central region (figure S1). For the heterojunction

photodetector, an FTO/glass substrate with a dimension of 3 cm × 7.5 cm was used. Chemical-etched grooves of different dimensions were created in the middle of the substrate. Subsequently, the substrate is placed on a spin coater, and 250 microliters of titanium oxide solution are carefully dispensed onto the rotating substrate at 4000 rpm. Before this stage, one of the electrodes (the conducting area of the FTO glass) and a small section of the etched area are shielded with adhesive tape to ensure that the wet titanium oxide layer covers only a specific part of the etched area, along with the other electrode. In the subsequent step, a layer of perovskite ink is applied through a similar process, spin-coated over the titanium oxide layer, and brought into contact with the other electrode. So the mesoporous TiO<sub>2</sub> layer was coated on one side of the groove, while the perovskite layer was deposited with one side overlapping the TiO<sub>2</sub> layer and the other edge covering the FTO/glass. After the application of each layer, a thermal post-treatment process is carried out. Four grooves with widths of 8 mm, 5 mm, 3 mm, and 1 mm were considered, but the 1 mm groove was not suitable as the head dimension of the homemade slot-die machine was not appropriate. Therefore, the TiO<sub>2</sub> and perovskite layers met both edges of the FTO/glass.

To evaluate the performance of the devices, current–voltage ( $I$ – $V$ ) measurements were conducted on both photodetectors using a potentiostat–galvanostat ( $\mu$ Auto lab) under varying intensities of UV illumination. The  $I$ – $V$  measurements were performed over a bias voltage range of  $-3$  V to 3 V, and the results were recorded after the same duration of storage time. Additionally, to assess the dynamic response of the photodetectors, a pulsed UV wavelength of 5 mW cm<sup>-2</sup> intensity was applied with a bias voltage of 3 V to measure the transient photocurrent.

### 2.3. Fabrication and measurement of a TENG

To enable the self-powering of the heterojunction TiO<sub>2</sub>/TCHMP photodetector, we fabricated an integrated TENG by using the FTO layer as the triboelectric layer in contact with Kapton. The tapping device with a frequency of 2 Hz was used to control the motion of the two electrodes, and the photodetector was powered by tapping the FTO contact to the Kapton/Al triboelectric layer. The voltage and current of the TENG were measured using a digital oscilloscope (Agilent Technologies DSO1022A) and a potentiostat–galvanostat ( $\mu$ Auto-lab system, Metrohm), respectively.

### 2.4. Characterizations

The surface morphologies of the TiO<sub>2</sub> and perovskite layers were characterized using a field emission scanning electron microscope (FESEM, TESCAN MIRA3) and energy dispersive x-ray analysis (Oxford instrument). X-ray diffraction (XRD, X'Pert Pro, PANalytical) was conducted to investigate the crystallization and structural properties of the different layers. The optical properties were evaluated using Photo-luminescence (PL) spectroscopy (Avantas- Avaspec-2048-TEC) and UV-Vis spectroscopy (Lambda 950).

## 3. Result and discussion

### 3.1. Optimization of slot-die printing parameters

The optimization of the slot-die deposition process is essential in the TiO<sub>2</sub>/TCHMP structure as the perovskite layer serves as the primary light absorber under UV irradiation. Achieving the desired thickness of the light absorber layer is crucial for the performance of photodetector devices as the diffusion length of charge carriers is limited to a few hundred nanometers.

Various parameters can influence the thickness and uniformity of the TCHMP layer during slot-die deposition, including substrate temperature, precursor solution concentration, gap spacing between the slot-die head and substrate, and printing speed. To ensure temperature uniformity during printing, a two-layer heating pad with a 27 × 30 cm<sup>2</sup> geometry was utilized. A resistance wire was positioned between two thick steel plates to enhance temperature uniformity due to its high heat capacity.

To evaluate the quality of the TCHMP depositions, experiments were conducted at different deposition temperatures of 25 °C, 50 °C, and 70 °C, as shown in figure 3. The presence of yellow (figure 3(a)) and black (figure 3(c)) perovskite layers indicated the incomplete formation of the perovskite structure (leading to the formation of PbI<sub>2</sub>) or a failure to achieve a continuous layer, resulting in isolated areas, respectively. Therefore, all substrates were printed at 50 °C to achieve optimal results.

To investigate the effect of precursor concentration on the quality of the triple-cation mixed halide perovskite (TCMHP) layer, different concentrations ranging from 0.5 M to 1.5 M were tested. To optimize these parameters, the optimal speed range for printing was initially determined, spanning between 1 and 1.2 cm per second. Subsequently, to explore concentration's influence on layer quality, concentrations ranging from 0.3 to 2 M were employed. Our previous experimental findings revealed that concentration, in

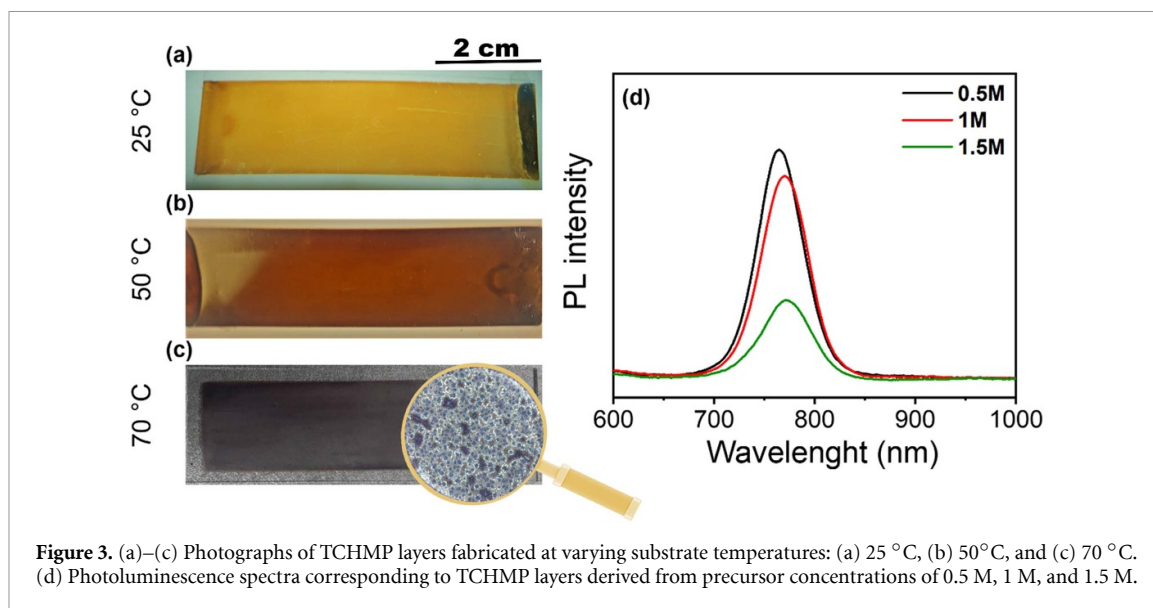


**Figure 3.** (a)–(c) Photographs of TCHMP layers fabricated at varying substrate temperatures: (a) 25 °C, (b) 50 °C, and (c) 70 °C. (d) Photoluminescence spectra corresponding to TCHMP layers derived from precursor concentrations of 0.5 M, 1 M, and 1.5 M.

terms of solvent evaporation, nucleation rate, and crystal growth, significantly affects layer quality [39]. Under the experimental conditions, lower concentrations yielded more consistent and desirable layer quality. However, concentrations below half a molar combined with a speed of  $1.2 \text{ cm s}^{-1}$  failed to generate the necessary thickness for the absorptive layer. Consequently, a minimum concentration of half a molar was chosen for the index layer within this speed range to fulfill the thickness requirement. To assess the quality of the printed layers, we initiated a comparison between the optical microscope images of the layers. Illustrated in figure S2, the reflective light microscope images of the three printed layers at concentrations of half, 1, and 1.5 molars are evident. It is discernible that the half-molar concentration demonstrates superior continuity and uniformity in comparison to the other layers. PL analysis was performed to assess the quality of the perovskite layer, as shown in figure 3(d). The results indicate that decreasing the precursor concentration to 0.5 M increased the PL of the TCMHP, which is associated with a decrease in non-optical recombination and improved film quality.

Subsequently, a TCMHP precursor concentration of 0.5 M was selected for the printing process, and the effect of the gap distance between the slot-die printing head and the substrate was studied. Figure 4(a) shows that varying the gap distances between  $100 \mu\text{m}$  to  $400 \mu\text{m}$  did not significantly affect the thickness of the TCMHP layer. Typically, an increase in the distance between the slot die head and the substrate results in a more pronounced stretching of the meniscus, leading to a decrease in internal pressure during the printing process. Conversely, narrowing the gap between the die slot head and the substrate amplifies internal pressure. This understanding underscores the critical role of the die gap height, also known as the coating gap, as a powerful optimization parameter for ensuring consistent coating processes across a wide range of pump rates, line speeds, and layer thicknesses. However, in our study, we observed that the gap between the slot die head and the substrate had minimal impact on sample thickness. This observation aligns with findings from other reports, which emphasize the importance of maintaining optimal meniscus liquid volume stability while minimizing the influence of substrate surface roughness [40–42]. As a result, we opted for a gap height of 200 micrometers in our research.

In the final step, the impact of slot-die head velocity on the thickness of the slot-die printed perovskite layer was investigated to optimize the thickness. As depicted in figure 4(b), the thickness of the solid film was observed to vary with the head velocity and two distinct regimes were identified. In region (I), the slow speed of the slot-die head ensures that the drying timescale is similar to the speed of movement. Consequently, solid particles amass at the meniscus, leading to the formation of a solid film. Conversely, region (II) represents the Landau-Levich regime. Here, the high shear stress, a byproduct of the rapid speed, results in wet layers remaining on the substrate post-printing. The schematic in figure 4(c) visually represents how variations in film thickness are governed by the relative speed difference between the head lip and the substrate. It should be noted that the graph's units are arbitrary due to the depiction's generalized nature. Additionally, while our representation pinpoints two primary coating regimes and an intermediate zone, the actual film thickness can be influenced by other parameters, such as the liquid's viscosity.

At a low coating speed, the thickness of the dry film is inversely affected by the speed, and solid particles accumulate under the meniscus. The thickness of the film decreases with increasing coating speed due to the

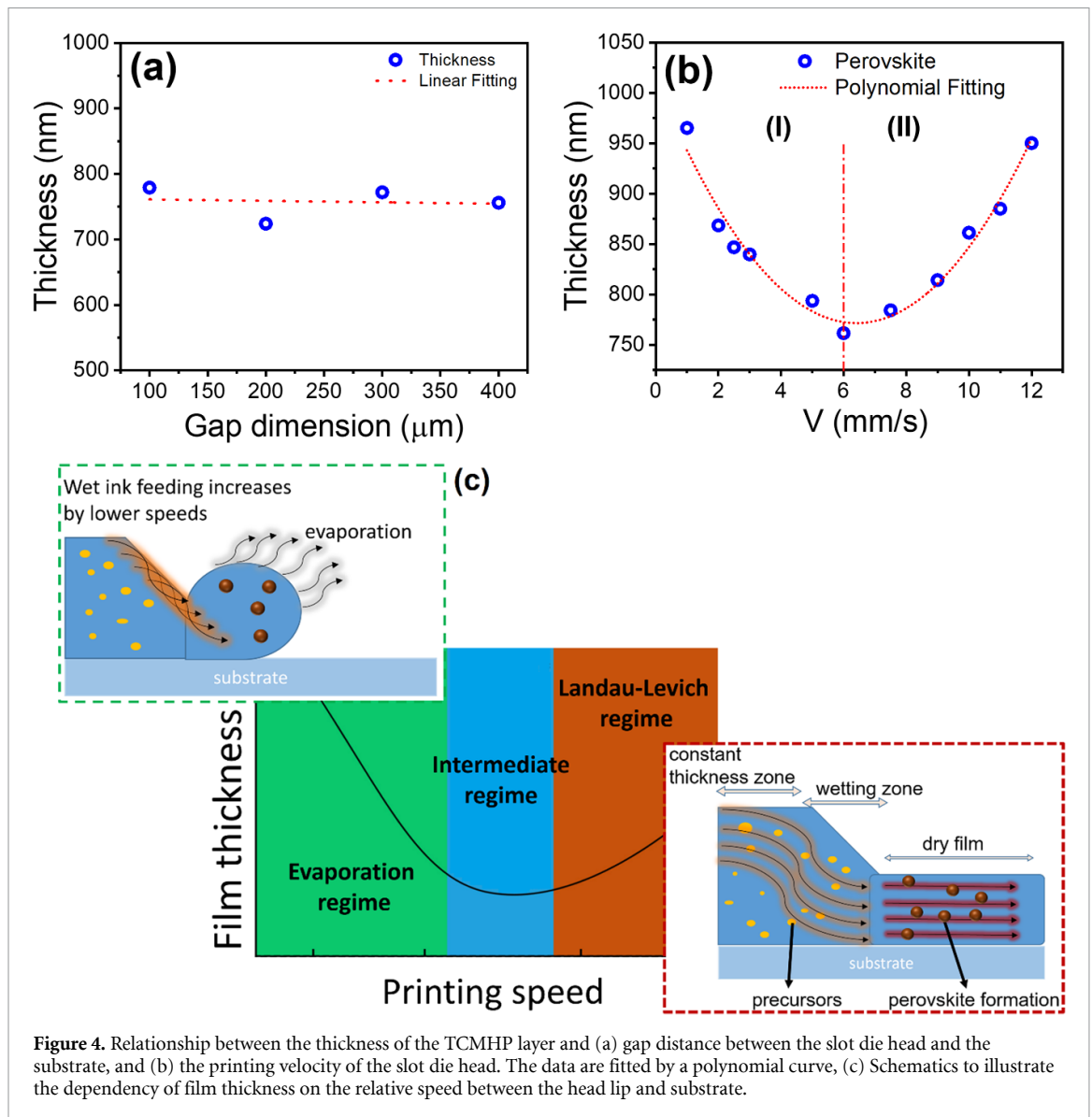


**Figure 4.** Relationship between the thickness of the TCMHP layer and (a) gap distance between the slot die head and the substrate, and (b) the printing velocity of the slot die head. The data are fitted by a polynomial curve, (c) Schematics to illustrate the dependency of film thickness on the relative speed between the head lip and substrate.

decreased time for the liquid to evaporate per unit length. Furthermore, drying in place leads to fluid flow toward the meniscus, which affects seed formation. Meanwhile, rapid solvent evaporation at the edges causes a phenomenon known as the coffee ring effect, which results in particles in the solution moving toward these regions and enhancing the growth of grain scale on a micrometer scale. Conversely, if the coating speed is too fast, the liquid does not have sufficient time to evaporate in the meniscus, and the coating process enters the Landau–Levich regime. However, the coated film in the Landau–Levich regime is desirable for mass production, as the thickness of the coated film increases with increasing speed. Nonetheless, there may also be a loss of coverage uniformity in this regime.

Table 1 displays the slot-die parameters utilized to achieve an optimized TCHMP layer with the desired thickness.

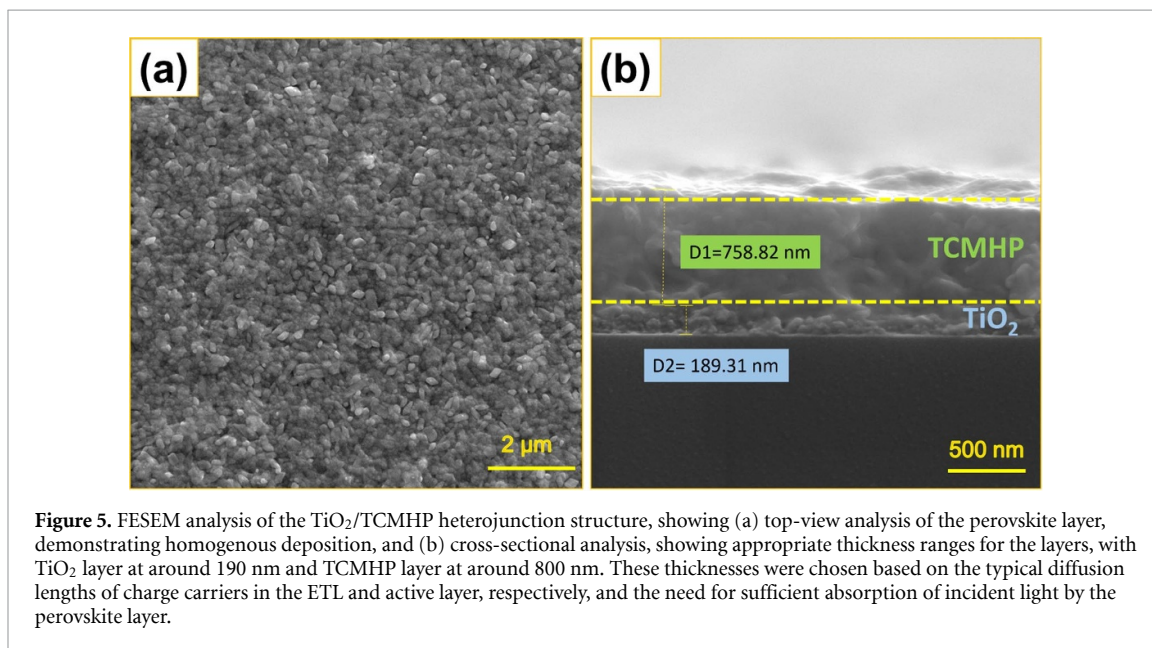
### 3.2. XRD and FESEM analysis

The XRD pattern of the perovskite layer is presented in figure S3. The detected peaks in this analysis confirm the formation of a crystalline TCMHP, namely  $(\text{FA}_{0.83} \text{MA}_{0.17})_{0.95} \text{Pb} (\text{I}_{0.83} \text{Br}_{0.17})_3$  (TCMHP). These crystalline peaks are consistent with prior research findings [43].

The FESEM analysis of the perovskite layer shows a homogeneous deposition, as presented in figure 5(a). The cross-sectional analysis of the  $\text{TiO}_2$ /TCMHP structure confirms the appropriate thickness ranges of the layers, approximately 190 nm and 800 nm for  $\text{TiO}_2$  and TCMHP layers, respectively (figure 5(b)). These thicknesses were selected based on the typical diffusion lengths of charge carriers in the electron transport layer (ETL) and active layer, respectively. Moreover, to absorb enough incident light, the perovskite layer

**Table 1.** Optimized slot-die deposition parameters for proper TCHMP layer thickness.

Criteria	Best value
Reservoir temperature	$25 \pm 5$ °C
Head temperature	$25 \pm 5$ °C
Substrate temperature	$35 \pm 5$ °C
Printing speed	$1\text{--}1.2$ cm s <sup>-1</sup>
Printing head type	Slot-die/roller printer
Slot-die shim	15 μm
Printing gap	200 μm
Post printing process	325 °C–500 °C in a predefined temperature profile
Substrate preparation	UV-ozone 15 min



should have a sufficient thickness, considering its high absorption coefficient of up to  $104\text{ cm}^{-1}$  [10]. To make perovskite a commercially viable absorber layer, its thickness should be within the range of 300 nm to 1000 nm. Based on the mean free path of carriers in the three-cation perovskite, an appropriate thickness range for the perovskite layer is around 800 nm [10].

### 3.3. TENG characterization

To enable the self-powered operation of the photodetector, a TENG was designed with a conductive connection between the FTO and Kapton triboelectric layers. Figure 6(a) shows the generated current of the FTO/Kapton TENG. The selection of FTO as an electrode in the photodetector's design is primarily driven by its role as the transparent conductive glass substrate. This choice was specifically made because of the integration of the NG energy source alongside the sensor. Furthermore, FTO, like many metals on the triboelectric series, is recognized for its strong electron-donating properties. Conversely, Kapton is positioned as an electron donor in the triboelectric series. This material possesses a wide array of intriguing characteristics, including its capability to withstand extreme temperatures, excellent mechanical properties, including wear resistance and flexibility, along commendable electrical characteristics. Additionally, it has been extensively employed in TENGs due to its proximity to the lower end of the triboelectric series [31, 32], enabling it to generate a substantial charge when it comes into contact with various materials including metals. These qualities are crucial considerations for practical applications. As illustrated in figure S4, when the triboelectric layers are in contact, positive and negative charges are generated in the FTO and Kapton layers, respectively, based on their electron affinities. Upon separation, induced positive charges are generated in the Al back contact layer due to charge induction, creating an electric current due to the difference in the electric charges in the FTO and Al layers. During the pressing process, the electrical charges are reversed, resulting in a reverse current. Figure 6(b) shows the current and voltage amplitude of the

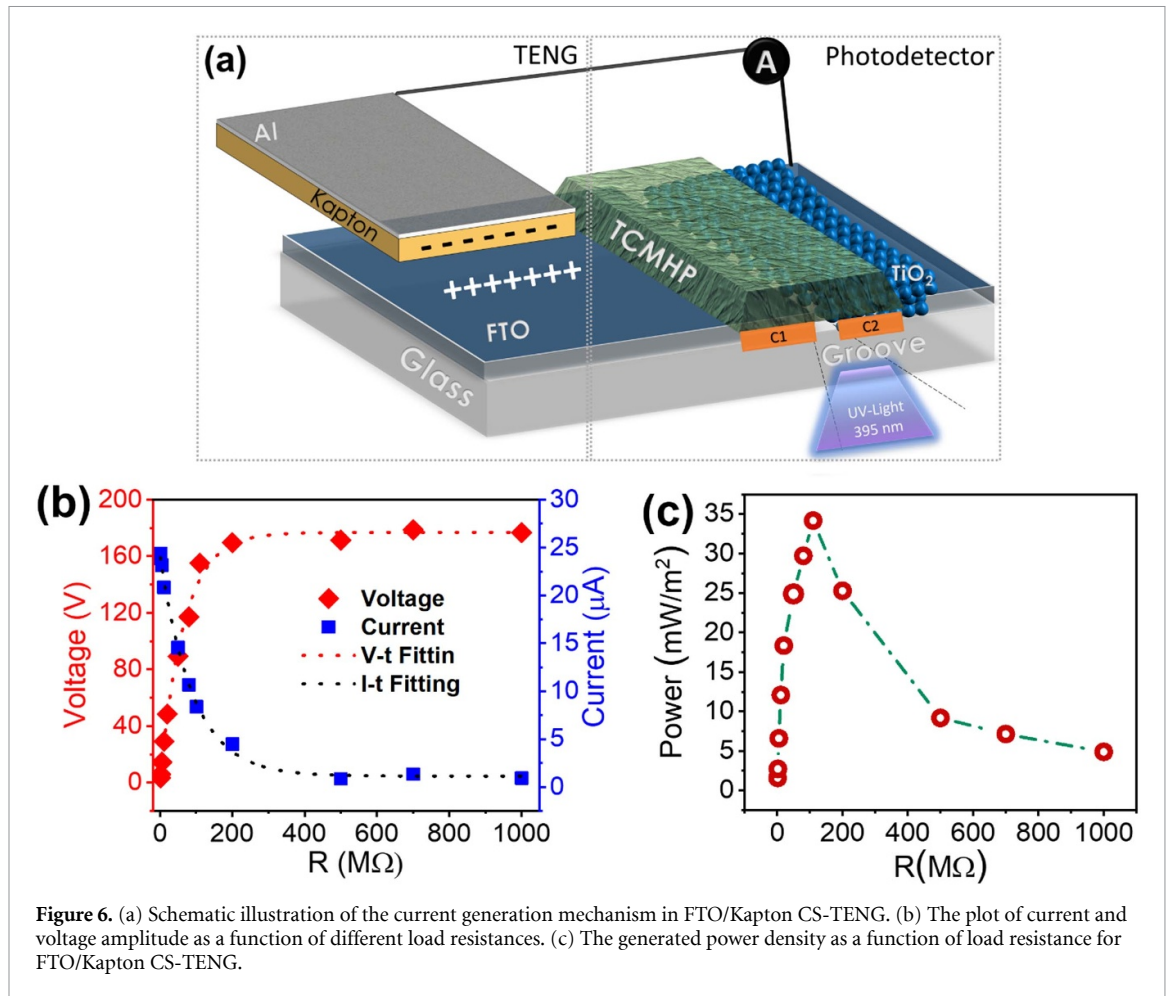


**Figure 6.** (a) Schematic illustration of the current generation mechanism in FTO/Kapton CS-TENG. (b) The plot of current and voltage amplitude as a function of different load resistances. (c) The generated power density as a function of load resistance for FTO/Kapton CS-TENG.

FTO/Kapton-based TENG with different load resistances of 1 M $\Omega$  to 1000 M $\Omega$  at a constant frequency of 2 Hz. The maximum power output of the TENG supply, calculated as  $P = V^2/RS$ , is about 34.18 mW m<sup>-2</sup> at a load resistance of 110 M $\Omega$ , as shown in figure 6(c). Here,  $V$  and  $R$  represent the output peak voltage across the external load and the load resistance, respectively, while  $S$  is the active surface of the TENG. The frequency-dependent behavior of TENG is illustrated in figure S5.

The long-term stability of the photodetector, particularly when powered by the NG, is a critical parameter for practical applications. To this end, the NG's durability was rigorously assessed through 350 tappings, as depicted in figure S6. Our observations indicate that the robust mechanical integrity of the layered surface significantly contributes to the consistent and unwavering output from the NG.

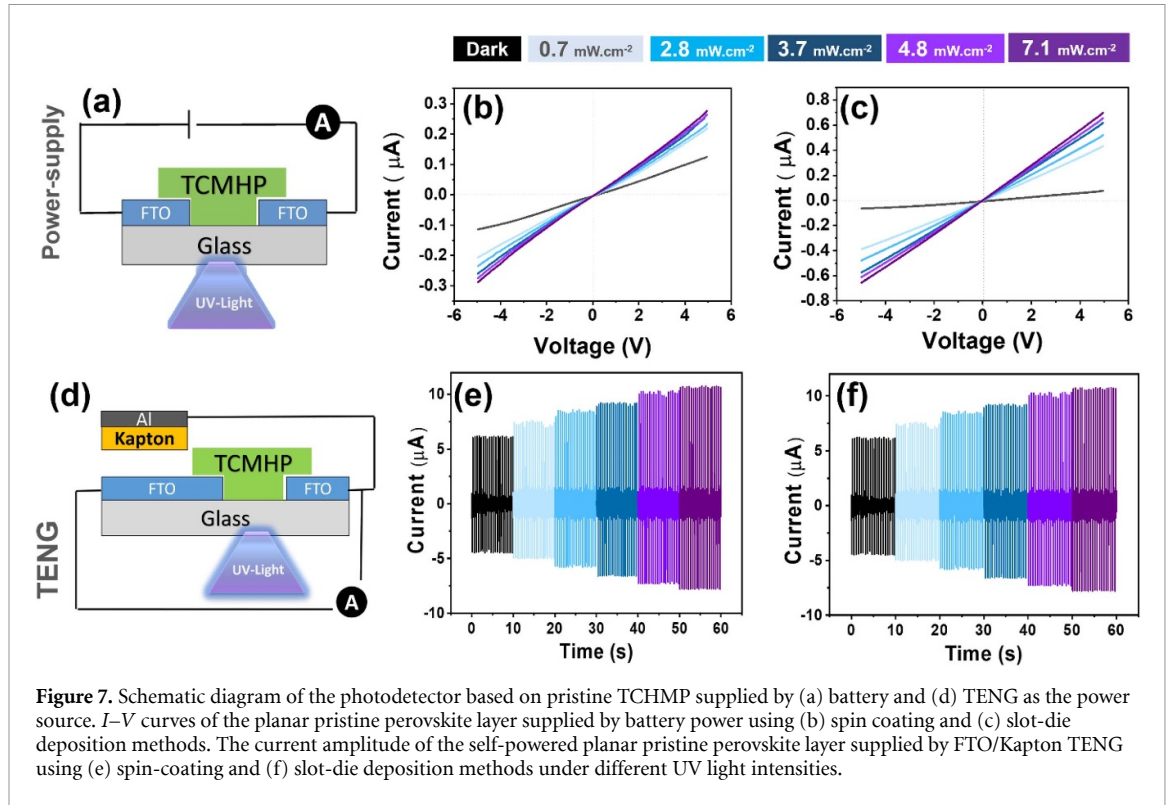
### 3.4. Characterization of photodetector performance

#### 3.4.1. Pristine perovskite-based photodetector

To investigate the suitability of slot die deposition for large-scale absorbance layer fabrication, perovskite material was deposited using both slot die and spin coating methods. The perovskite layer's optimized thickness for both deposition methods was found to be approximately 800 nm. Photodetector performance was evaluated using both a battery (figure 7(a)) and a TENG (figure 7(d)) as the power source.

For the realization of our self-powered device, we integrated the photodetector with the CS-FTO/Kapton TENG using an impedance-matching circuit. Generally, there are two prevalent methods to achieve a self-powered photodetector via TENG: the passive and the active approach. This work primarily employs the passive approach, which necessitates an impedance-matching circuit to harmonize the impedance of the TENG with that of the photodetector. Ensuring this compatibility is crucial for the seamless functionality of the device. The semi-logarithmic current versus load resistance graph for the CS-FTO/Kapton TENG shows that its effective resistance range spans from 5 M $\Omega$  to 300 M $\Omega$ , as depicted in figure S7. Notably, the resistance of our perovskite-based photodetector aligns within this active range, situated around tens of M $\Omega$ .

The current-voltage characteristics of the pristine perovskite-based photodetectors, prepared using both the spin coating and slot die methods, were evaluated under varying light intensities and are depicted in



figures 7(b) and (c), respectively. Furthermore, the self-powered pristine perovskite layer's behavior under different light intensities was investigated, and the results are shown in figures 7(e) and (f).

The results demonstrate that the current amplitude of the pristine perovskite-based devices produced through spin-coating and slot-die methods is comparable when using either battery or TENG as the power supply. However, to differentiate between the photodetectors, it is essential to calculate key parameters such as responsivity, detectivity, and external quantum efficiencies (EQEs). Responsivity measures the photocurrent generated per unit of incident optical power on the effective surface area, detectivity quantifies the sensitivity of the photodetector, and EQE represents the number of electrons generated per incident photon [44, 45].

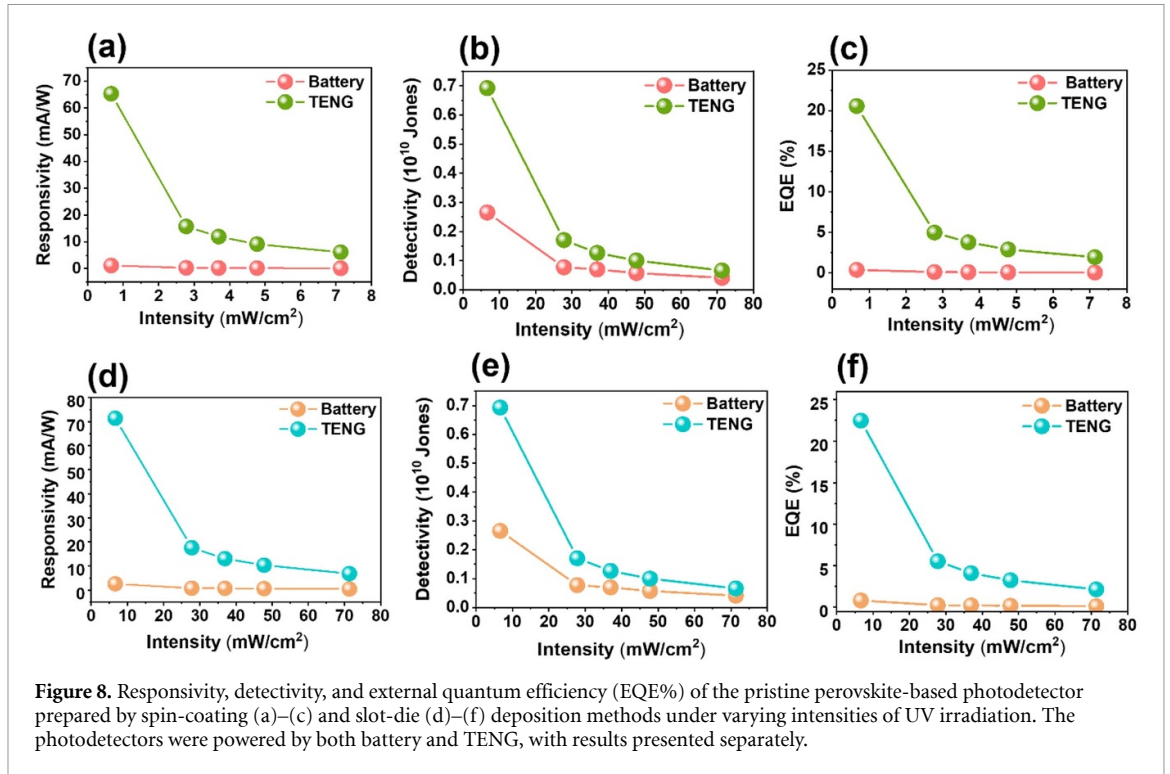
The effectiveness of the slot-die method for depositing a large-scale absorbance layer was evaluated by comparing it with the traditional spin-coating method. To differentiate between the photodetectors, key parameters such as responsivity, detectivity, and EQEs were calculated. These parameters were calculated using equations (1)–(3):

$$R = \frac{I_{ph}}{P_0} \quad (1)$$

$$D^* = \frac{RS^{1/2}}{(2eI_d)^{1/2}} \quad (2)$$

$$EQE = \frac{hcR\lambda}{e\lambda} \quad (3)$$

where  $I_{ph}$  and  $I_d$  are the current amplitudes in the light and dark situations, respectively,  $P_0$  is the light intensity,  $S$  is the effective area over which light is illuminated,  $e$  is the elementary charge,  $h$  is Planck's constant,  $c$  is the velocity of light, and  $\lambda$  is the wavelength of the incident light. The results, shown in figures 8(a)–(f), indicate that the slot-die method is a more suitable process for preparing optoelectronic devices compared to the traditional spin-coating method. The highest values of  $R$ ,  $D^*$ , and EQE for the self-powered TCMHP photodetector supplied by the FTO/Kapton TENG were 71.4 (mA W<sup>-1</sup>),  $6.93 \times 10^{10}$  Jones, and 22.5%, respectively. Moreover, the slot-die method has the advantage of reducing the precursor compared to the spin-coating method. These findings suggest that the slot-die method is promising for developing optoelectronics on a semi-industrial scale in terms of both precursor consumption and device



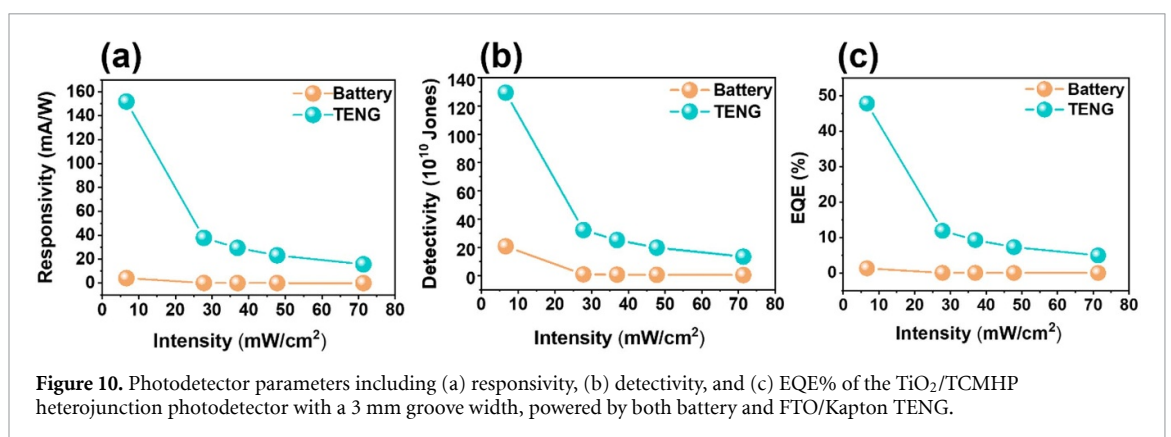
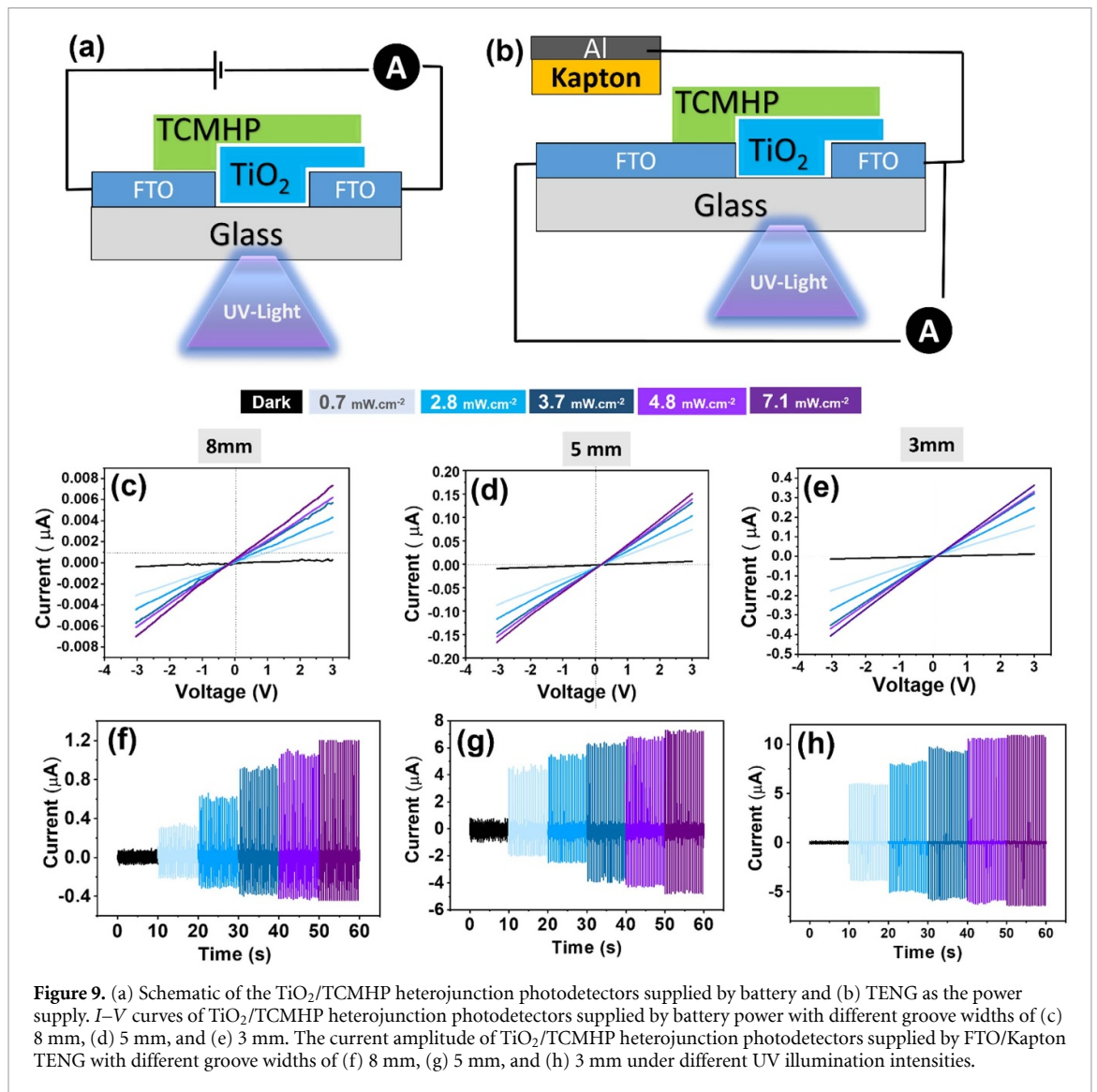
performance. In figures 8(a)–(f), the photodetector’s parameters display a decrease as the light intensity rises. This observed reduction in responsivity at higher light intensities can be attributed to the filling of electron traps, leading to an increase in electron-hole recombination. As the traps become saturated with electrons, there’s a consequential rise in the quasi-Fermi level, thereby increasing the number of free electrons in the system. As the illumination intensity escalates, the likelihood of electron-hole recombination similarly grows, influencing other parameters closely tied to responsivity [35]. In contrast, when the photodetector is powered by a battery, the consistent voltage supply might offset some of the effects of increased recombination, leading to a relatively stable responsivity even at higher light intensities. Conversely, with TENG-powered devices, the variability in energy supply might exacerbate the observed reduction in performance at elevated light intensities.

### 3.4.2. $\text{TiO}_2/\text{TCMHP}$ -based photodetectors

The slot-die method allows for the fabrication of a  $\text{TiO}_2/\text{TCMHP}$  heterojunction structure without the need for a mask. To further evaluate its effectiveness, the performance of UV-PDs with different groove dimensions (8 mm, 5 mm, and 3 mm) was investigated under the battery and TENG power supply (figure 9). The current diversity versus applied voltage for battery-powered heterostructure  $\text{TiO}_2/\text{TCMHP}$  photodetectors was analyzed and the transient current of self-powered  $\text{TiO}_2/\text{TCMHP}$  PD supplied by the FTO/Kapton TENG at various light intensities for different groove dimensions was characterized.

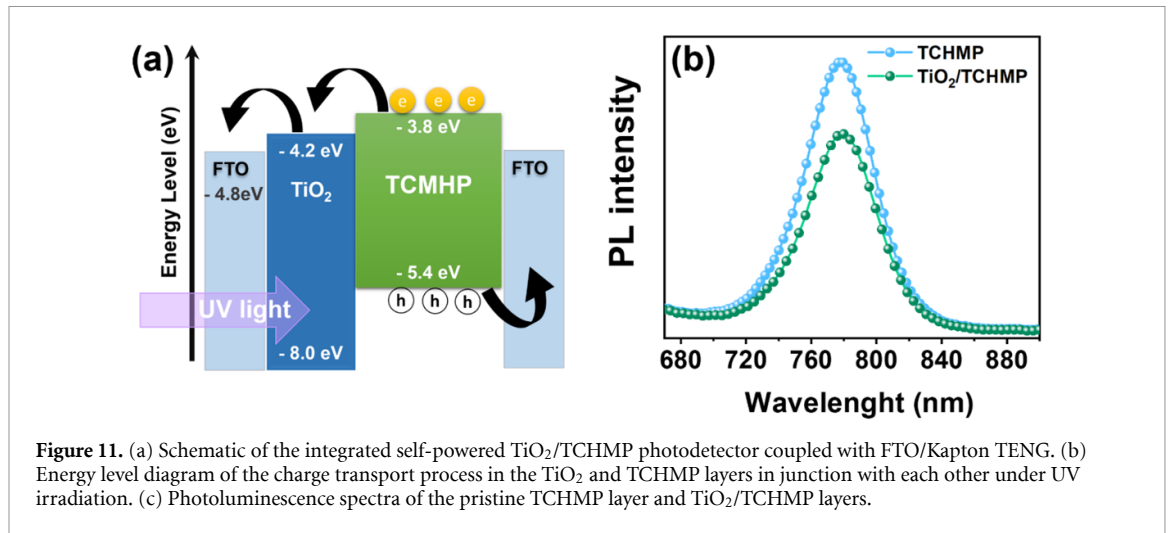
The reduction of the etched groove width in  $\text{TiO}_2/\text{TCMHP}$  photodetectors resulted in enhanced current amplitudes for both battery and FTO/Kapton TENG-powered devices. This was due to a decrease in electron-hole recombination rate, allowing more carriers to reach the FTO substrates as electrical contacts and thus improving output signals. The 3 mm groove width was found to be the optimal design for a large, high-performance photodetector coupled with TENG. The optimized  $\text{TiO}_2/\text{TCMHP}$  photodetector showed a significant improvement in responsivity, detectivity, and EQE% compared to the pristine TCHMP-based photodetector (figure 10). Under UV illumination of  $0.7 \text{ mW cm}^{-2}$ , the highest values of  $R$ ,  $D^*$ , and EQE were  $151.9 \text{ mA cm}^{-2}$ ,  $1.29 \times 10^{11}$  Jones, and 47.83%, respectively. The improved responsivity and detectivity of the self-powered  $\text{TiO}_2/\text{TCMHP}$  heterojunction compared to the self-powered pristine TCHMP-based photodetector were 212.9% and 124.5%, respectively, due to better charge carrier separation and transportation to electrical contacts.

The stability of PDs is a critical factor that requires careful investigation. In this study, we evaluated the stability of the  $\text{TiO}_2/\text{TCMHP}$  heterojunction PDs under on/off UV-irradiation with an intensity of  $5 \text{ mW cm}^{-2}$  (figure S8(a)). The rising and falling times of the proposed  $\text{TiO}_2/\text{TCMHP}$  PDs were calculated based on changes in the current under illumination. The rising time was determined as the time required for



the current to increase from 10% to 90% under illumination, while the falling time was determined as the time required for the current to decrease from 90% to 10% when the illumination was turned off. Results showed that the rising time and falling time for the TiO<sub>2</sub>/perovskite PD with a 3 mm groove width were approximately 0.80 s and 0.42 s, respectively (figures S8(b) and (c)).

The responsivity, detectivity, and EQE% of the photodetector powered by the TENG show a significant improvement compared to that powered by a battery (figures 8(a)–(f) and 10(a)–(c)). This phenomenon is likely related to the nature of TENG properties. In the proposed self-powered coupling circuit, the



photodetector acts as the load resistance for the TENG (figure 6(a)), and upon light illumination, the resistance of the photodetector decreases, leading to changes in the TENG properties. In contrast, in the case of optical sensor operates on battery power, the voltage at both ends of the sensor remains nearly constant. This consistency is attributed to the battery's internal characteristics, characterized by low resistance and high stability throughout its operation, even as the current passing through the optical sensor varies in response to changes in light intensity. Furthermore, the current amplitude of the  $\text{TiO}_2/\text{TCHMP}$  also increases under light illumination due to the reduction in the photodetector's resistance. The synergy between the TENG's properties and the current amplitude in the circuit results in improved performance of the self-powered PD coupled with the TENG, as reported recently by Ejehi *et al* [46]. In practical scenarios, random motions with diverse frequencies and forces lead to variations in output pulses, impacting the sensor's performance. This challenge is inherent to all pulsed output NGs. Nonetheless, certain circuitry solutions are available to convert these pulsed outputs to DC [37, 46]. To achieve this objective, we can connect the output of the compact NG to an electrolytic capacitor. In this configuration, owing to the low internal resistance of the electrolytic capacitor, the electrical loads transferred to the capacitor plates can serve as a stable voltage power source after a certain period, resulting in minimal voltage fluctuations. Consequently, we have harnessed the output power of the TENG generated through random tapping and stored it in a  $20 \mu\text{F}$  capacitor connected in parallel to a photodetector. As illustrated in figure S9, when exposed to light, the charging voltage of the capacitor exhibits reduced sensitivity to the TENG's random power fluctuations, quickly stabilizing within a few seconds.

The energy level diagram (figure 11(a)) provides insight into the mechanism of charge transport in the  $\text{TiO}_2/\text{TCHMP}$  layer. The  $\text{TiO}_2$  functions as the ETL and TCHMP as the hole transport layer. Upon light illumination, electron-hole pairs are created, and a strong potential forms between the junction, enhancing charge carrier separation and decreasing charge carrier recombination. This was confirmed by studying the PL spectra of the TCHMP films with and without an MP  $\text{TiO}_2$  layer. As shown in figure 11(b), the PL intensity of the TCHMP/ $\text{TiO}_2$  distinctly decreased compared to the pristine TCHMP layer, suggesting that the spontaneous radiative recombination of TCHMP was passivated, leading to improved charge separation and transfer at the MP- $\text{TiO}_2/\text{TCHMP}$  interface.

To investigate the effect of the MP  $\text{TiO}_2$  layer on the heterojunction-based photodetector further, the  $I-V$  curves of the device were studied (figure S10). The difference in current amplitude between the device in the dark and under high-intensity UV irradiation (about  $7.8 \text{ mW cm}^{-2}$ ) was not significant. This is due to the large bandgap of the  $\text{TiO}_2$  layer, which limits its optical absorption even under UV wavelength irradiation and leads to low photocurrent production. Additionally, the wide bandgap of the  $\text{TiO}_2$  causes rapid electron-hole recombination, decreasing photocurrent conversion efficiency [43, 45]. The presented  $I-V$  curve underscores that the optical absorption of  $\text{TiO}_2$  exerts a negligible impact on the photodetector's performance. The notable improvement in PD operation is predominantly attributed to enhancements in charge transfer efficiency. The heterojunction  $\text{TiO}_2/\text{TCHMP}$  structure is more practical for photodetector design than single perovskite or single  $\text{TiO}_2$ -based photodetectors because it enables proper energy level design.

The performance of the proposed self-powered  $\text{TiO}_2/\text{TCHMP}$  PD structure was assessed by comparing it with other self-powered perovskite-based PDs supplied by NGs, such as piezoelectric NGs (PENGs) and

**Table 2.** Comparison of output signals of self-powered perovskite-based photodetectors supplied by different nanogenerators.

Self-powered PD structure	Power source	Wavelength & light intensity			Sensitivity	Responsivity	References
PET/ITO/MAPbI <sub>3</sub> -PVDF/Carbon tape	PENG	UV (462 nm) & 42.25 mW cm <sup>-2</sup>	44 nA	80 nA	0.82	—	[47]
FTO/FAPbBr <sub>3</sub> -PVDF/Ag	PENG	1 Sun & 100 mW cm <sup>-2</sup>	26.2 V	16.1 V	0.39	—	[48]
ITO/ CsPbI <sub>3</sub> -PVDF composite/ITO	PENG	1 Sun & 100 mW cm <sup>-2</sup>	5 μA	11.6 μA	1.32	0.3 mA W <sup>-1</sup>	[49]
FTO/CsPbBr <sub>3</sub> /Carbon/Ag	TENG	1 Sun & 100 mW cm <sup>-2</sup>	0.3 μA	270 μA	899.00	—	[50]
FTO/compact TiO <sub>2</sub> /mesoporous TiO <sub>2</sub> +CH <sub>3</sub> NH <sub>3</sub> PbI <sub>3</sub> /CH <sub>3</sub> NH <sub>3</sub> PbI <sub>3</sub>	TENG	1 Sun & 100 mW cm <sup>-2</sup>	4 V	3 V	0.25	0.75 V W <sup>-1</sup>	[33]
FTO/TiO <sub>2</sub> /MAPbI <sub>3</sub> /PTFE/Cu	TENG	1 Sun & 100 mW cm <sup>-2</sup>	0.18 μA	0.2 μA	0.11	—	[34]
FTO/TiO <sub>2</sub> /MAPbI <sub>3</sub> -x/Pentacene//PTFE/Al	TENG	1 Sun & 100 mW cm <sup>2</sup>	0.61 μA	0.92 μA	0.51	0.22 mA W <sup>-1</sup>	[51]
FTO/SnS <sub>2</sub> /Cs <sub>0.05</sub> (FA <sub>0.83</sub> MA <sub>0.17</sub> ) <sub>0.95</sub> Pb(I <sub>0.83</sub> Br <sub>0.17</sub> ) <sub>3</sub>	TENG	1 Sun & 10 mW cm <sup>-2</sup>	0.39 μA	1.2 μA	2.02	0.2 A/W	[37]
FTO							
FTO/TiO <sub>2</sub> /TCHMP/FTO	TENG	UV (395 nm) & 0.66 mW cm <sup>-2</sup>	0.01 μA	94.8 μA	9479.00	0.15 A/W	This work

TENGs (table 2). Sensitivity parameters, which indicate the light-to-dark current ratio, were analyzed to determine their responsiveness. The results were compiled into a comparison table, which showed that the TCHMP heterojunction coupled with TENG had the highest sensitivity and responsivity among the different structures. The successful fabrication of the PD using the slot-die method holds great promise for the development of semi-industrial devices with improved efficiency.

#### 4. Conclusion

In this study, we investigated the performance of a TiO<sub>2</sub>/TCHMP heterojunction photodetector fabricated using the slot-die method. We found that the optimized device with a 3 mm groove width coupled with a TENG showed significantly improved responsivity, detectivity, and EQE% compared to the pristine TCHMP-based photodetector. The stability of the device was also demonstrated under on/off UV irradiation.

Our results indicate that the slot-die method is a promising approach for developing optoelectronic devices on a semi-industrial scale. Additionally, the coupling of the heterojunction photodetector with a TENG resulted in enhanced device performance due to changes in TENG properties and improved charge carrier separation and transfer at the MP-TiO<sub>2</sub>/TCHMP interface.

Comparative studies with other self-powered perovskite-based photodetectors demonstrated that the proposed TiO<sub>2</sub>/TCHMP heterojunction PD had the highest sensitivity and responsivity among the different structures supplied by different NGs.

In conclusion, this study demonstrates the potential of the slot-die method and TiO<sub>2</sub>/TCHMP heterojunction structure for the development of high-performance self-powered photodetectors with applications in fields such as environmental monitoring, security surveillance, and health care. Further research is needed to optimize and scale up the fabrication process and to explore additional applications for this promising technology.

#### Data availability statement

The data cannot be made publicly available upon publication because they are not available in a format that is sufficiently accessible or reusable by other researchers. The data that support the findings of this study are available upon reasonable request from the authors.

#### ORCID iDs

Raheleh Mohammadpour  <https://orcid.org/0000-0002-6596-0622>

Nima Taghavinia  <https://orcid.org/0000-0003-1138-6917>

Daryoosh Vashaee  <https://orcid.org/0000-0003-3667-3672>

## References

- [1] Bouilly-Gauthier D, Jeannes C, Maubert Y, Duteil L, Queille-Roussel C, Piccardi N, Montastier C, Manissier P, Piérard G and Ortonne J-P 2010 Clinical evidence of benefits of a dietary supplement containing probiotic and carotenoids on ultraviolet-induced skin damage *Br. J. Dermatol.* **163** 536–43
- [2] Behar-Cohen F, Baillet G, de Agyuavives T, Garcia P O, Krutmann J, Peña-García P, Reme C and Wolffsohn J S 2013 Ultraviolet damage to the eye revisited: eye-sun protection factor (E-SPF®), a new ultraviolet protection label for eyewear *Clin. Ophthalmol.* **8** 87–104
- [3] Alamdari S, Sasani Ghamsari M, Lee C, Han W, Park H-H, Tafreshi M J, Afarideh H and Ara M H M 2020 Preparation and characterization of zinc oxide nanoparticles using leaf extract of *Sambucus ebulus* *Appl. Sci.* **10** 3620
- [4] Fang X, Hu L, Huo K, Gao B, Zhao L, Liao M, Chu P K, Bando Y and Golberg D 2011 New ultraviolet photodetector based on individual Nb<sub>2</sub>O<sub>5</sub> nanobelts *Adv. Funct. Mater.* **21** 3907–15
- [5] Talip M A A, Khairir N S, Kadir R A, Mamat M H, Rani R A, Mahmood M R and Zoolfakar A S 2019 Nanotubular Ta<sub>2</sub>O<sub>5</sub> as ultraviolet (UV) photodetector *J. Mater. Sci., Mater. Electron.* **30** 4953–66
- [6] Bintsis T, Litopoulou-Tzanetaki E and Robinson R K 2000 Existing and potential applications of ultraviolet light in the food industry—a critical review *J. Sci. Food Agric.* **80** 637–45
- [7] Choudhary R and Bandla S 2012 Ultraviolet pasteurization for food industry *Int. J. Food Sci. Nutrition Eng.* **2** 12–15
- [8] Chen J, Ouyang W, Yang W, He J H and Fang X 2020 Recent progress of heterojunction ultraviolet photodetectors: materials, integrations, and applications *Adv. Funct. Mater.* **30** 1909909
- [9] Al-Amri A M, Cheng B and He J-H 2018 Perovskite methylammonium lead trihalide heterostructures: *progress and challenges IEEE Trans. Nanotechnol.* **18** 1–12
- [10] Han X, Wu W, Chen H, Peng D, Qiu L, Yan P and Pan C 2021 Metal halide perovskite arrays: from construction to optoelectronic applications *Adv. Funct. Mater.* **31** 2005230
- [11] Xu Y and Lin Q 2020 Photodetectors based on solution-processable semiconductors: recent advances and perspectives *Appl. Phys. Rev.* **7** 011315
- [12] Qian C-X, Deng Z-Y, Yang K, Feng J, Wang M-Z, Yang Z, Liu S (F) and Feng H-J 2018 Interface engineering of CsPbBr<sub>3</sub>/TiO<sub>2</sub> heterostructure with enhanced optoelectronic properties for all-inorganic perovskite solar cells *Appl. Phys. Lett.* **112** 093901
- [13] Tan H et al 2017 Efficient and stable solution-processed planar perovskite solar cells via contact passivation *Science* **355** 722–6
- [14] Wu H, Zhang C, Ding K, Wang L, Gao Y and Yang J 2017 Efficient planar heterojunction perovskite solar cells fabricated by in-situ thermal-annealing doctor blading in ambient condition *Org. Electron.* **45** 302–7
- [15] Heo J H, Lee M H, Jang M H and Im S H 2016 Highly efficient CH<sub>3</sub> NH<sub>3</sub> PbI<sub>3-x</sub>Cl<sub>x</sub> mixed halide perovskite solar cells prepared by re-dissolution and crystal grain growth via spray coating *J. Mater. Chem. A* **4** 17636–42
- [16] Li S-G, Jiang K-J, Su M-J, Cui X-P, Huang J-H, Zhang -Q-Q, Zhou X-Q, Yang L-M and Song Y-L 2015 Inkjet printing of CH<sub>3</sub> NH<sub>3</sub> PbI<sub>3</sub> on a mesoscopic TiO<sub>2</sub> film for highly efficient perovskite solar cells *J. Mater. Chem. A* **3** 9092–7
- [17] Tong S et al 2019 Fully-printed, flexible cesium-doped triple cation perovskite photodetector *Appl. Mater. Today* **15** 389–97
- [18] Wang R, Kwon H-J, Tang X, Ye H, Park C E, Kim J, Kong H and Kim S H 2020 Slot-die coating of sol-gel-based organic-inorganic nano-hybrid dielectric layers for flexible and large-area organic thin film transistors *Appl. Surf. Sci.* **529** 147198
- [19] Gao L, Huang K, Long C, Zeng F, Liu B and Yang J 2020 Fully slot-die-coated perovskite solar cells in ambient condition *Appl. Phys. A* **126** 1–7
- [20] Gong C, Tong S, Huang K, Li H, Huang H, Zhang J and Yang J 2020 Flexible planar heterojunction perovskite solar cells fabricated via sequential roll-to-roll microgravure printing and slot-die coating deposition *Solar RRL* **4** 1900204
- [21] Shi Q, Dong B, He T, Sun Z, Zhu J, Zhang Z and Lee C 2020 Progress in wearable electronics/photonics—moving toward the era of artificial intelligence and internet of things *InfoMat* **2** 1131–62
- [22] Chen Y et al 2021 A review of lithium-ion battery safety concerns: the issues, strategies, and testing standards *J. Energy Chem.* **59** 83–99
- [23] Kim J-E, Jung Y-S, Heo Y-J, Hwang K, Qin T, Kim D-Y and Vak D 2018 Slot die coated planar perovskite solar cells via blowing and heating assisted one step deposition *Sol. Energy Mater. Sol. Cells* **179** 80–86
- [24] Zhang Y, Yang F, Guo Q, Feng X, Duan Y, Guo J, Cheng G and Du Z 2022 The self-powered photodetector of n-Si/n-ZnO heterojunction with enhanced temperature adaptability via transient current response *J. Appl. Phys.* **55** 504004
- [25] Ippili S, Jella V, Thomas A M and Yoon S-G 2021 The recent progress on halide perovskite-based self-powered sensors enabled by piezoelectric and triboelectric effects *Nanoenergy Adv.* **1** 3–31
- [26] Hinchet R, Yoon H-J, Ryu H, Kim M-K, Choi E-K, Kim D-S and Kim S-W 2019 Transcutaneous ultrasound energy harvesting using capacitive triboelectric technology *Science* **365** 491–4
- [27] Shwon S M A Z et al 2021 Piezo-tribo dual effect hybrid nanogenerators for health monitoring *Nano Energy* **82** 105691
- [28] Naval S, Verma P, Jain A and Mallick D 2023 Hybrid vector and pressure sensor for fingertip dynamics sensing using DC-triboelectric/AC-piezoelectric mechanisms *Sens. Actuators A* **355** 114330
- [29] Naval S, Beigh N T, Mukherjee D, Jain A and Mallick D 2022 Flexible V-shaped piezoelectric-triboelectric device for biomechanical energy harvesting and sensing *J. Appl. Phys.* **55** 365501
- [30] Munirathinam P, Mathew A A, Shanmugasundaram V, Vivekananthan V, Purusothaman Y, Kim S-J and Chandrasekhar A 2023 A comprehensive review on triboelectric nanogenerators based on real-time applications in energy harvesting and self-powered sensing *Mater. Sci. Eng. B* **297** 116762
- [31] Luo J and Wang Z L 2020 Recent progress of triboelectric nanogenerators: from fundamental theory to practical applications *EcoMat* **2** e12059
- [32] Su L, Zhao Z X, Li H Y, Yuan J, Wang Z L, Cao G Z and Zhu G 2015 High-performance organolead halide perovskite-based self-powered triboelectric photodetector *ACS Nano* **9** 11310–6
- [33] Su L, Zhao Z, Li H, Wang Y, Kuang S, Cao G, Wang Z and Zhu G 2016 Photoinduced enhancement of a triboelectric nanogenerator based on an organolead halide perovskite *J. Mater. Chem. C* **4** 10395–9
- [34] Leung S F, Ho K T, Kung P K, Hsiao V K, Alshareef H N, Wang Z L and He J-H 2018 A self-powered and flexible organometallic halide perovskite photodetector with very high detectivity *Adv. Mater.* **30** 1704611
- [35] Wang Y, Duan J, Yang X, Liu L, Zhao L and Tang Q 2020 The unique dielectricity of inorganic perovskites toward high-performance triboelectric nanogenerators *Nano Energy* **69** 104418
- [36] Wang F, Ahmad S, Al Mdallal Q, Alammari M, Khan M N and Rehman A 2022 Natural bio-convective flow of Maxwell nanofluid over an exponentially stretching surface with slip effect and convective boundary condition *Sci. Rep.* **12** 2220

- [37] Shooshtari L, Ghods S, Mohammadpour R, Esfandiar A and Iraj Zad A 2022 Design of effective self-powered SnS<sub>2</sub>/halide perovskite photo-detection system based on triboelectric nanogenerator by regarding circuit impedance *Sci. Rep.* **12** 7227
- [38] Naval S, Jain A and Mallick D 2022 Direct current triboelectric nanogenerators: a review *J. Micromech. Microeng.* **33** 013001
- [39] Triana S and Suryana R 2016 Effect of wet etching process on the morphology and transmittance of fluorine doped tin oxide (FTO) *J. Phys.: Conf. Ser.* **776** 012005
- [40] Mahmoodpour S, Heydari M, Shooshtari L, Khosroshahi R, Mohammadpour R and Taghavinia N 2023 Slot-die coated copper indium disulfide as hole-transport material for perovskite solar cells *Sustainability* **15** 6562
- [41] Chang H M, Chang Y R, Lin C F and Liu T J 2007 Comparison of vertical and horizontal slot die coatings *Polym. Eng. Sci.* **47** 1927–36
- [42] Chang Y-R, Chang H-M, Lin C-F, Liu T-J and Wu P-Y 2007 Three minimum wet thickness regions of slot die coating *J. Colloid. Interface Sci.* **308** 222–30
- [43] Wang K, Liao Y, Li W, Zhang Y, Zhou X, Wu C, Chen R and Kim T W 2023 Triboelectric nanogenerator module for circuit design and simulation *Nano Energy* **107** 108139
- [44] Shooshtari L, Esfandiar A, Orooji Y, Samadpour M and Rahighi R 2021 Ultrafast and stable planar photodetector based on SnS<sub>2</sub> nanosheets/perovskite structure *Sci. Rep.* **11** 19353
- [45] Linsebigler A L, Lu G and Yates J T Jr 1995 Photocatalysis on TiO<sub>2</sub> surfaces: principles, mechanisms, and selected results *Chem. Rev.* **95** 735–58
- [46] Ejehi F, Shooshtari L, Mohammadpour R, Asadian E and Sasanpour P 2022 Self-powered ultraviolet/visible photodetector based on graphene-oxide via triboelectric nanogenerators performing by finger tapping *Nanotechnology* **33** 475205
- [47] Sultana A, Sadhukhan P, Alam M M, Das S, Middy T R and Mandal D 2018 Organo-lead halide perovskite induced electroactive β-phase in porous PVDF films: an excellent material for photoactive piezoelectric energy harvester and photodetector *ACS Appl. Mater. Interfaces* **10** 4121–30
- [48] Hsiao V K, Leung S-F, Hsiao Y-C, Kung P-K, Lai Y-C, Lin Z-H, Salama K N, Alshareef H N, Wang Z L and He J-H 2019 Photo-carrier extraction by triboelectricity for carrier transport layer-free photodetectors *Nano Energy* **65** 103958
- [49] Maity K, Pal U, Mishra H K, Maji P, Sadhukhan P, Mallick Z, Das S, Mondal B and Mandal D 2022 Piezo-phototronic effect in highly stable CsPbI<sub>3</sub>-PVDF composite for self-powered nanogenerator and photodetector *Nano Energy* **92** 106743
- [50] Wang Y, Yang X, Yu X, Duan J, Yang Q, Duan Y and Tang Q 2020 Triboelectric charging behaviors and photoinduced enhancement of alkaline earth ions doped inorganic perovskite triboelectric nanogenerators *Nano Energy* **77** 105280
- [51] Yang X D et al 2019 Robust perovskite-based triboelectric nanogenerator enhanced by broadband light and interface engineering *J. Mater. Sci.* **54** 9004–16